Desalination 593 (2025) 118217

Contents lists available at ScienceDirect

Desalination

journal homepage: www.elsevier.com/locate/desal

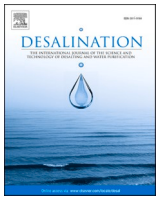

Optimized performance of membrane-based desalination by high-throughput molecular dynamic simulations and machine learning analysis

Jinji Cao [a], Zhaoqin Xu [a], Mingjie Wei [a,*], Lihan Li [b], Bin Wu [b], Yong Wang [a,c]

[a] State Key Laboratory of Materials-Oriented Chemical Engineering, and College of Chemical Engineering, Nanjing Tech University, Nanjing 211816, Jiangsu, China
[b] School of Economics and Management, Nanjing Tech University, Nanjing 211816, Jiangsu, China
[c] School of Energy and Environment, Southeast University, Nanjing 210096, Jiangsu, China

HIGHLIGHTS

- Optimized desalination performance is obtained by HTMD simulations & ML analysis.
- Influence of pore size on water permeance is revealed from molecular level.
- Effect of hydrophilicity on water permeance is also coupled with pore size.
- Ion rejection of CNTs to NaCl is interactively affected by σ, ε, and Δ*P*.
- Δ*P* has very little impact on water permeance as flux rises linearly with it.

GRAPHICAL ABSTRACT

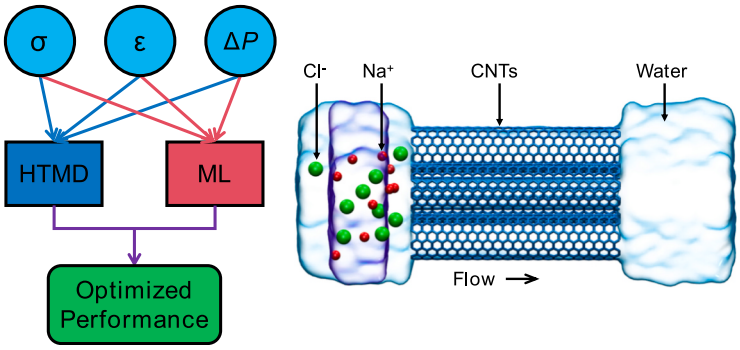

ARTICLE INFO

Keywords:
Desalination
High-throughput molecular dynamics
Hydrophilicity
Pore size
Machine learning

ABSTRACT

The influence of pore size and hydrophilicity on the permeance of reverse osmosis (RO) membranes has been mostly focused. However, their influence is hardly to be clearly identified as these two kinds of factor interfere with each other. In this work, high-throughput molecular dynamics (HTMD) simulations with CNTs are used to extensively produce the data of water permeance and NaCl rejection. These data are then analyzed by machine learning (ML) method to obtain the optimized desalination performance. The HTMD results indicate that the pressure drop has little effect on the water permeance. Moreover, rising pore size and degrading hydrophilicity will generally boost water permeance but will somehow sacrifice the NaCl rejection. The interference effect between pore size and hydrophilicity is also found in this work, the mechanism of which is then revealed from molecular level. Additionally, ML is applied to analyze the abundant data of water permeance and NaCl rejection. The optimal conditions are identified to achieve the highest water permeance with 100% NaCl rejection, which are also validated *via* additional MD simulations. This work suggests that the integration of HTMD and ML promises the future of designing new kind of RO membranes for better performance.

* Corresponding author.
E-mail address: mj.wei@njtech.edu.cn (M. Wei).

https://doi.org/10.1016/j.desal.2024.118217
Received 13 July 2024; Received in revised form 20 September 2024; Accepted 15 October 2024
Available online 23 October 2024

1. Introduction

Freshwater scarcity has emerged as a pressing global issue due to rapid population growth, industrialization, and the escalating impacts of climate change, such as global warming. In response, desalination has gained widespread adoption as an effective solution [1–4]. While reverse osmosis (RO) technology is the most prevalent method [5–7], it faces significant challenges, *e.g.* high energy consumption [8–10], susceptibility to fouling, and limited lifespan [11]. Carbon nanotubes (CNTs) have emerged as a promising alternative following Hummer et al.'s discovery of rapid water channels through molecular dynamics (MD) simulations [12]. Majumder et al. later confirmed experimentally that water flux in CNTs exceeds predictions by the Hagen-Poiseuille (HP) equation by three to four orders of magnitude [13].

However, large-scale fabrication of vertically aligned CNTs remains a complex and costly endeavor in experimental settings [14]. Although the preparation of CNT RO membranes is commercially impractical, CNTs have become an ideal material for studying desalination due to their simple structure and outstanding water transport performance [15–17]. Consequently, computational simulation methods have emerged as pivotal tools for investigating desalination of CNTs.

Using CNTs as models, researchers often employ modifications to explore how different structural, physical, and chemical properties influence desalination performance. Corry conducted MD simulations by modifying functional groups with varying charges and polarities at the entrance of (8) CNT pores [18]. These modifications demonstrated that altering functional groups at the pore mouth can enhance salt rejection through electrostatic and size effects. Similarly, Goldsmith et al. utilized MD simulations to adjust the atomic charges of CNTs across different pore sizes, revealing that these modifications led to reduced water flux compared to unmodified CNTs, though still higher than predicted by HP eq. [19].

The hydrophilicity of CNTs can be tailored by adjusting the charge on carbon atoms or fine-tuning interactions between carbon and oxygen atoms in water molecules. Ebrahimi et al. investigated the influence of varying water-CNT wall interaction strength on the spontaneous entrance of water into CNTs. They found a direct correlation between the distance of oxygen atoms in water molecules near the wall and carbon atoms in CNTs, influenced by σ values in the potential function [20]. Additionally, Joseph et al. adjusted CNTs' Lennard-Jones parameters near silicon to enhance hydrophilicity, resulting in increased water transport resistance and markedly reduced water flux [21]. Moreover, Wang et al. explored modifications in atomic charges of (12) CNTs for hydrophilic enhancements, observing a decrease in water flux post-modification compared to unmodified CNTs, though still significantly 11–21 times higher than predictions from Navier-Stokes eqs. [22].

Based on the findings from above works, we could conclude that the adjusting of interaction parameters between oxygen atom in water and carbon atom in CNTs can switch the effective pore size and hydrophilicity of CNTs rapidly. That reminders us that we could conduct high-throughput molecular dynamics (HTMD) simulations by adjusting interaction parameters in our simulations. HTMD simulations are particularly adept at depicting the transport dynamics of water molecules and salt ions at the nanoscale, capable of swiftly generating vast datasets. With these abundant data, machine learning (ML) algorithms subsequently uncover meaningful patterns to predict material efficiency. Wang et al. proposed a pioneering approach that melds deep reinforcement learning with convolutional neural networks to expedite the discovery of graphene nanopores suitable for desalination [23]. Meanwhile, Liang et al. have accelerated the assessment of graphene's desalination potential using HTMD coupled with ML techniques [24]. By integrating HTMD simulations with ML, researchers can effectively and precisely analyze and predict the desalination capabilities of CNTs. This cohesive approach not only bypasses the practical limitations of experimental methods but also accelerates the discovery and optimization of new materials.

In this work, we integrate HTMD and ML techniques to analyze the desalination performances of RO membranes based on the CNT models. It explores the impacts of pressure drops (ΔP), CNTs pore size and hydrophilicity on water permeance and ion rejection performance of CNT membranes. The extensive HTMD simulations generate comprehensive data on water permeance and ion rejection, which are then evaluated and predicted using ML methods. For the goal of identifying optimal CNTs conditions that achieve 100% ion rejection while maximizing permeance, ML algorithms are applied and provide its predictions, which are also validated by additional MD simulations. The approach applied in this work not only thoroughly examines the influence of ΔP, pore size, and hydrophilicity of CNTs on the permeance and desalination performance but also introduces novel methodologies for enhancing desalination materials.

2. Simulation details

2.1. Construction of models

Taking the (8) CNT model as an example, the simulation configuration is shown in Fig. 1. Each simulation consists of four (8) CNTs arranged in a rhombus shape (shown in Fig. 1). The interval between CNTs is set to 0.1 nm, which can prevent water and ion from transporting membranes *via* these intervals [25]. The length of the tube is 5 nm. A NaCl solution of concentration at 1 mol/L is placed on the left, and a reservoir of pure water is placed on the right. The diameters of the (8) and (9) armchair-type CNTs correspond to 1.08 nm and 1.22 nm, respectively. After subtracting the van der Waals diameter of the carbon atoms (0.34 nm), the effective diameters are 0.74 nm and 0.88 nm, respectively. The simulation box is rhombic with a side length of 2.51 nm and a height of 2.17 nm. The size in the z-direction varies with the simulation conditions. The axis of the CNTs is parallel to the z-direction, and the initial lengths of the two reservoir boxes in the z-direction are set to 2.50 nm.

2.2. Simulation methods

All simulations are performed using the large-scale atomic/molecular massively parallel simulator (LAMMPS) program [26]. The CNTs are held fixed, and water molecules are modeled using the SPC/E model [27], with the SHAKE algorithm used to constrain the bond length and bond angle of water molecules to accelerate the simulation speed [28]. The cutoff radius for Lennard-Jones (LJ) and electrostatic interactions is set to 1.0 nm and 1.2 nm, respectively. Long-range electrostatic forces are calculated using the Particle-Particle Particle-Mesh (PPPM) method with a precision of 10^{-4} [29]. The simulation system exhibited periodic boundary conditions in all three directions. The LJ parameters between oxygen atoms in water molecules and carbon atoms on the CNTs utilized the parameters proposed by Werder et al. with: $\sigma_{C\text{-}O} = 3.19$ Å, $\varepsilon_{C\text{-}O} = 0.392$ kJ mol^{-1} [30]. The parameters for Na^+ and Cl^- are based on the parameters proposed by Joung et al. [31]. All other cross LJ interaction parameters are calculated using the Lorentz-Berthelot mixing rule.

The LJ potential function is a commonly used potential energy function that describes the interactions between molecules or atoms. It is a function of the distance between two atoms, with two parameters σ and ε, and its form is as follows:

$$V(r) = 4\varepsilon\left[\left(\frac{\sigma}{r}\right)^{12} - \left(\frac{\sigma}{r}\right)^{6}\right] \quad (1)$$

where r is the distance between two atoms, ε is the depth of the potential well, and σ is the distance at which the potential energy between the two interacts is exactly zero, typically defined as the closest distance of approach between the two atoms.

Each simulation system undergoes an initial energy minimization (with a precision of 10^{-5}) followed by equilibration MD simulations at

300 K to ensure that the CNTs are filled with water molecules. Subsequently, non-equilibrium molecular dynamics (NEMD) simulations are performed. Using the "pump method" [32–35], an external force f is applied to all oxygen atoms of water molecules within a 1 nm wide region on the left side of the CNTs (the purple area in Fig. 1a), resulting in the generation of ΔP. The calculation formula is as:

$$f = \frac{\Delta PA}{n} \tag{2}$$

where ΔP is the required pressure difference, A is the surface area of the model, and n is the number of water molecules in the selected region. The value of ΔP ranges from 100 to 300 MPa, significantly higher than the experimental ΔP, as the higher ΔP enhances signal-to-noise ratio and speeds up the simulation process [36,37]. The system temperature and pressure are controlled at 300 K and 300 MPa, respectively, using the Nosé-Hoover thermostat and Parrinello-Rahman barostat, while removing the influence of the particle center-of-mass velocity on temperature. The NEMD simulation duration is 3 ns with a time step of 1 fs. The initial 1 ns is dedicated to achieving system equilibrium, while the subsequent 2 ns are used for calculating flux and rejection data.

When computing the self-diffusion coefficient of water molecules within the nanopores, ions and water boxes outside the pores are excluded, and the nanopores are filled with water molecules. The simulation box size is set to match the dimensions of the CNTs, with periodic boundary conditions applied in all three directions. The simulation runs for 2 ns under the NVT ensemble, with a time step of 1 fs, and trajectory files are collected.

2.3. HTMD simulation

The HTMD simulation method, which is employed in this work, offers significant computational speed advantages over traditional MD simulations, enabling the completion of simulation tasks in a shorter time. Its highly automated workflow significantly simplifies operational steps and facilitates the straightforward handling of large-scale simulation data, providing a more comprehensive information basis for further analysis [38].

Fig. 2 illustrates the implementation of high throughput computation based on LAMMPS. By adding two conditional statements in the input file, it is possible to respectively modify σ and ε for carbon atoms in CNTs and oxygen atoms in water, to adjust the pore size and hydrophilicity of CNTs, respectively. For each simulation, we firstly define initial values, then read the model and perform equilibrium MD simulations. After that we perform NEMD to generate trajectory files and flux data of water and ions. Finally, we reset all parameters to the initial state using the "clear" command.

The HTMD simulations are performed by a double loop. In the inner loop, the variation of ε is adjusted, where ε values range from e/8 to 8e (where $e = \varepsilon_{C\text{-}O} = 0.392$ kJ mol^{-1}). ε is doubled from one to the other. After 7 loops, ε reaches 8e. Subsequently, the outer loop for σ is performed, with ε reset to the initial value e/8. The σ range changes for (8) CNTs from 2.19 Å to 4.99 Å and for (9) CNTs from 2.59 Å to 4.99 Å,

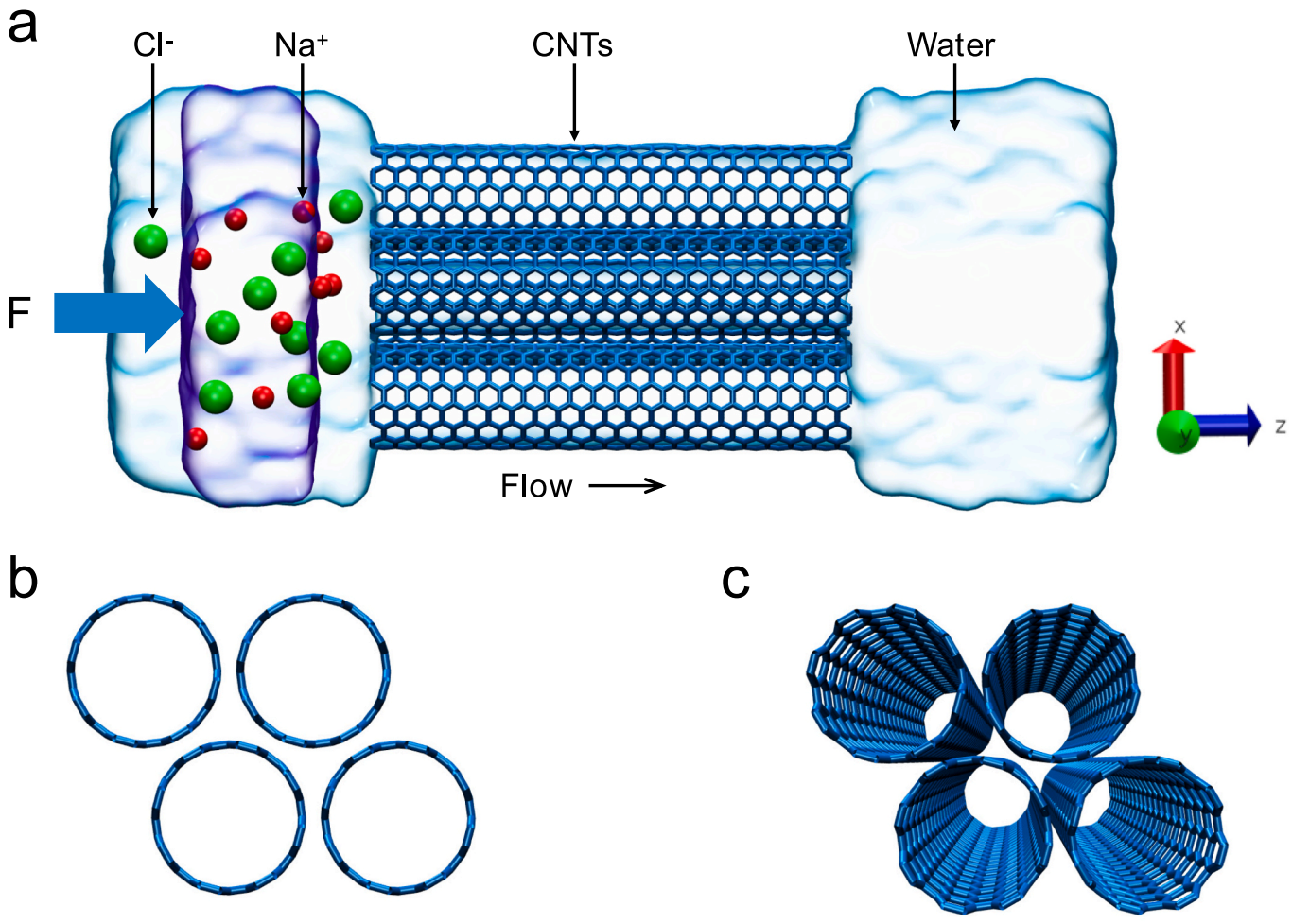

Fig. 1. Schematic diagram of the simulation model: (a) Simulation model of water molecules transporting in the (8) CNTs. External force is applied to the water molecules within the purple area. (b) Rhombic arrangement diagram of CNTs. (c) Perspective arrangement diagram of CNTs. All elements are labeled in the legend.

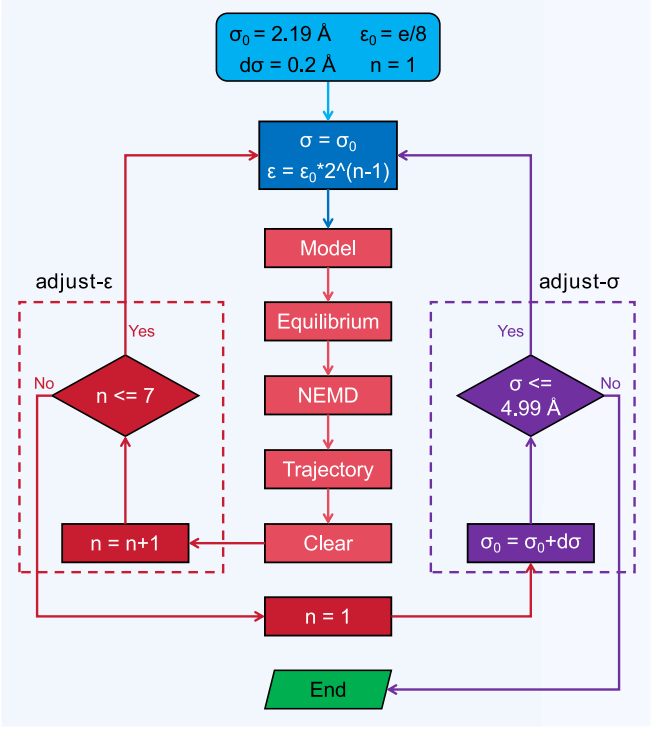

Fig. 2. Flowchart of the HTMD simulation running in LAMMPS.

increasing σ by 0.2 Å each iteration. By the double-loop simulations, at least 91 sets of data are obtained for one submission.

3. Results and discussion

3.1. The influence of ΔP on permeance

HTMD simulations are employed to investigate the permeance and NaCl rejection performance of two types of CNTs, (8) and (9), under Δ*P* of 100, 200, and 300 MPa. After HTMD simulations, 270 and 234 sets of valid data are obtained for (8) and (9) CNTs, respectively, which can serve as the database for the subsequent ML section. The permeance of water in these CNTs is depicted in Fig. 3. It is evident from the graph that water molecules exhibit high permeance primarily in regions with smaller σ and ε values. Moreover, increasing Δ*P* does not lead to significant changes in permeance. Since permeance is calculated by dividing water flux by Δ*P*, we plot the dependence of flux on Δ*P* as shown in Fig. 4. Three different σ values are selected for (8) and (9) CNTs, and their dependence of water flux on Δ*P* exhibits a linear relationship passing through the origin. This finding precisely aligns with Darcy's law, indicating that Δ*P* takes little effect on the permeance.

After excluding the influence of Δ*P*, we then focus on the effects of pore size (σ) and hydrophilicity (ε) variations on the permeation and salt rejection performance of CNTs. Consequently, the variation of water molecule permeance with σ and ε is plotted for (8) and (9) CNTs (shown in Fig. 5), in which Δ*P* of 100 MPa is selected. The permeance of water molecules gradually increases overall as the pore size increases (drop of σ). However, this increase is not strictly monotonic. Such phenomena will be discussed in subsequent sections. Additionally, as hydrophilicity increases (ε increases), the permeance of water molecules shows a monotonically decreasing trend. As the hydrophilicity promotion elevates the mass transport resistance of water molecules across the CNTs, a decrease in permeance is obtained [39]. In the coming sections, we will then analyze the influence of pore size and hydrophilicity on permeance one by one and then consider these two factors together by ML.

3.2. The impact of pore size on permeance

The influence of varying pore size (σ) on the permeance of both types of CNTs is investigated while keeping ε unchanged. Taking ε = e as an example, it's evident that changing σ has a significant impact on permeance (as shown in Fig. 6). In the case of (8) CNTs, when σ decreases from 4.79 to 2.99 Å, the permeance remains around 1000 L/(m^2 h bar) (LMHB). However, as σ decreases further to 2.39 Å, the permeance rapidly increases from 1360.18 to 5967.40 LMHB. Similarly, for (9) CNTs, when σ decreases from 4.79 to 3.39 Å, the permeance stays around 1000 LMHB. Yet, as σ decreases further to 2.79 Å, the permeance rapidly increases from 1190.29 to 5011.19 LMHB. Summarizing the permeance trends of these two types of CNTs, it can be observed that with an increase in σ, the permeance initially drops sharply, followed by oscillatory decreases. Such phenomena were also found by other simulation works [40]. The oscillatory permeance of water as a function of pore size was also observed in experimental works [41].

In order to further clarify the factors influencing permeance, the LJ potential function in Eq. (1) is analyzed. In the potential energy

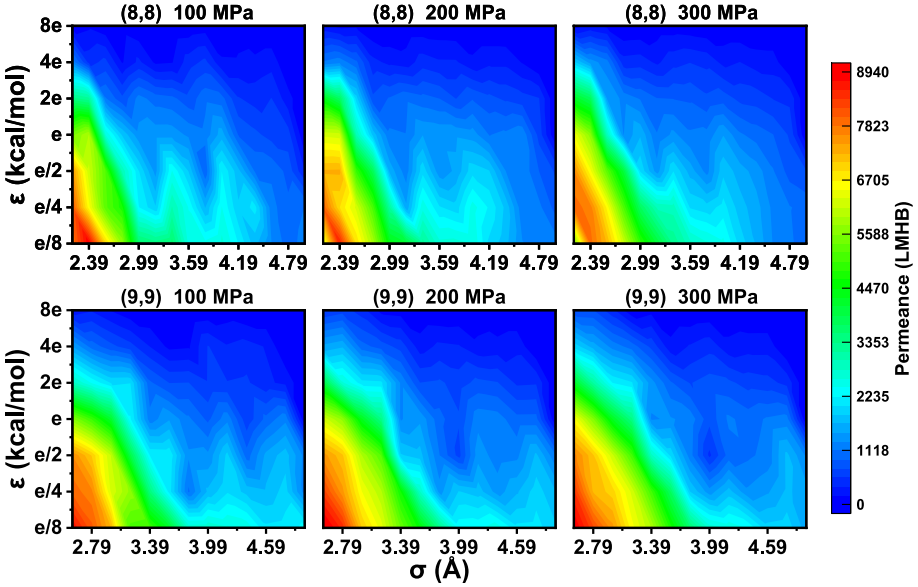

Fig. 3. Variation of permeance of (8) and (9) CNTs in high-throughput molecular dynamics simulations with respect to Δ*P*, σ, and ε.

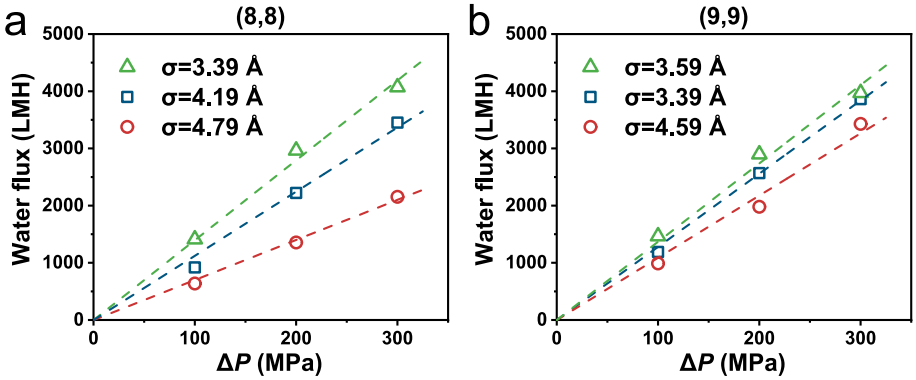

Fig. 4. Water flux of (8) (a) and (9) CNTs at different σ under various pressures.

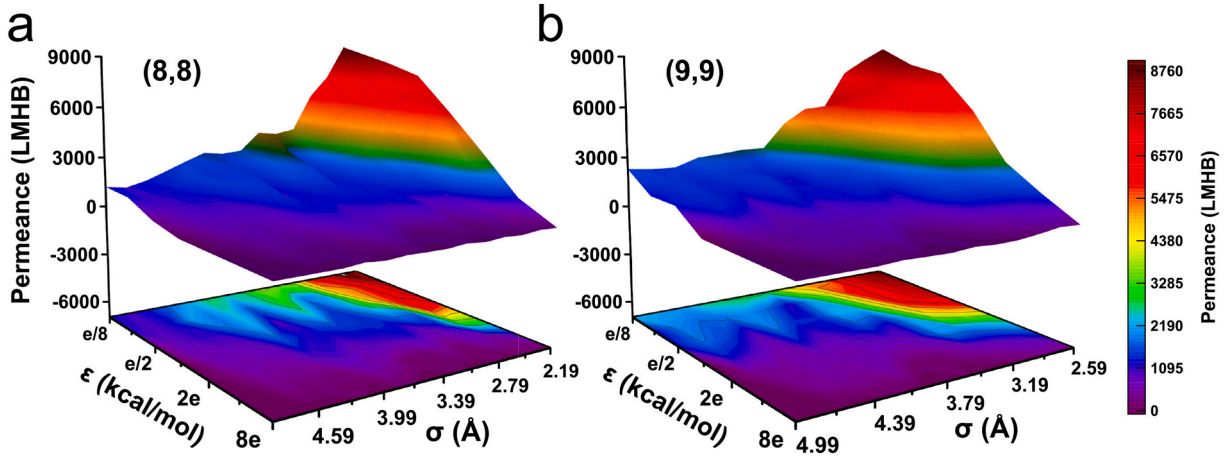

Fig. 5. Permeance of (8) and (9) CNTs as a function of σ and ε at 100 MPa.

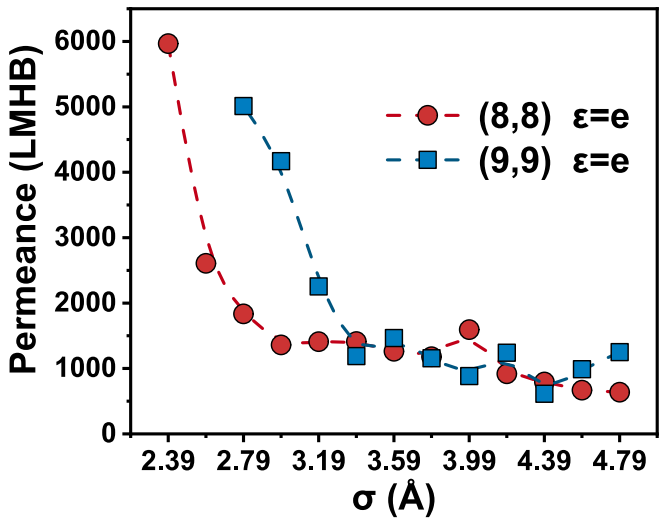

Fig. 6. Permeance variation curves of (8) and (9) CNTs as a function of σ.

function, σ is a length parameter representing the distance between two atoms where the potential energy is at its minimum, indicating the closest distance between the two atoms, such as between C and O. Six different σ values are selected for (8) (Fig. 7a) and (9,9) (Fig. 7b) CNTs to examine the variation in the diameter of water rings formed by internal oxygen atoms.

For the CNTs with similar pore size, the water molecules form a structure like a ring inside CNTs [42]. In (8) CNTs of this work, as σ increases from 2.79 to 4.79 Å, the diameter of the internal water ring decreases from 7.5 to 4.3 Å. The diameter of the water ring inside both types of CNTs decreases with increasing σ, indicating that changing σ can alter the effective diameter of the CNTs. When σ increases, the minimum distance between C and O increases, corresponding to a decrease in the effective diameter of the CNTs and thus a reduction in the diameter of the water ring formed inside them. Such reduction will consequently lead to the decreased water permeance.

When the diameter of the water ring is larger than 6.1 Å, an additional density peak appears inside the water ring, indicating a transition in the water molecule structure from one-ring configuration to "ring + dot" structure inside the CNTs. This is a result of the increased water density. In Fig. 7, the diameter of the water ring decreases as σ increases, and the color of the water ring becomes darker as σ increases, indicating that changing σ affects the structure of water molecules as well as their number inside CNTs.

Figs. 8 show the variation in the number of water molecules inside two types of CNTs with changing σ, while keeping ε constant. In the (8) CNTs, as σ increases from 2.39 to 4.79 Å, the number of water molecules decreases from 461 to 89. The planar density of water molecules, calculated based on the diameter of the water ring, increases from 2.99 to 4.19 #/Å^2 while σ increases from 2.39 to 3.19 Å, and then oscillates around 4.5 #/Å^2 as σ continues to increase from 3.39 to 4.79 Å (shown in Fig. 8a). In the (9) CNTs, as σ increases from 2.79 to 4.79 Å, the number of water molecules decreases from 537 to 228. The planar density of water molecules increases from 3.04 to 4.01 #/Å^2 while σ is no larger than 3.59 Å, and then oscillates around 4 #/Å^2 as σ continues to increase from 3.59 to 4.79 Å (shown in Fig. 8b).

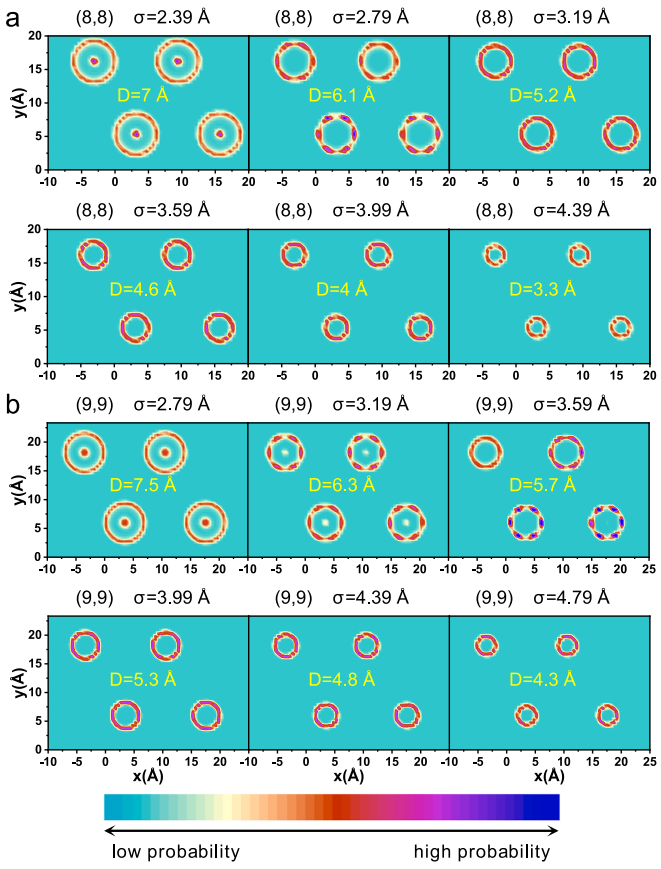

Fig. 7. The *xy*-plane density maps for oxygen atoms of water inside CNTs of (8) and (9) CNTs at different σ values.

For both types of CNTs, the number of water molecules gradually decreases with increasing σ. Additionally, the planar density of water molecules initially increases and then oscillates with increasing σ. This explains the reason for the color of the water ring in Fig. 7 decreases first and then remains unchanged with the increase of σ.

In order to further investigate the reason for varying diameters of water rings, we then focus on the microstructure of water ring inside CNTs. Thomas et al. demonstrated that water molecules exhibit stacked pentagonal structures in (8) CNTs and stacked hexagonal arrangements in (9) CNTs [42]. In Fig. 9a, for (8) CNTs, at σ = 2.39 Å, water molecules inside CNTs show disordered bulk water structures. At σ = 2.79 and 3.19 Å, water molecules inside CNTs exhibit stacked pentagonal structures. They become stacked tetrahedral structures at σ = 3.59 Å, triangular structures at σ = 3.99 Å, and double water chains at σ = 4.39 Å.

In Fig. 9b, for (9) CNTs, at σ = 2.79 Å, water molecules inside CNTs show disordered bulk water structures, indicating that the exchange of water between "ring" and "dot" is frequent. At σ = 3.19 Å, water molecules inside CNTs display stacked hexagonal structures with a single water chain at the center of the water ring. At σ = 3.59 Å, they exhibit stacked hexagonal structures. They become stacked pentagonal structures at σ = 3.99 Å, tetrahedral structures at σ = 4.39 Å, and triangular structures at σ = 4.79 Å. This indicates that the number of water chains formed inside CNTs decreases with increasing σ while ε is kept constant.

Comparing Figs. 8 with Fig. 6, the sharp decrease of water permeance cannot be explained by the water density inside CNTs. We then calculate the flow rate of water molecules inside CNTs (shown in Fig. 10a). In the (8) CNTs, as σ increases from 2.39 to 2.79 Å, the flow rate of water decreases from 2.75 to 1.12 m/s, and then oscillates around 1.4 m/s as σ continues to increase. In the (9) CNTs, as σ increases from 2.79 to 3.59 Å, the flow rate of water decreases from 3.39 to 0.89 m/s, and then oscillates around 1.3 m/s as σ continues to increase. This trend is similar to that in Fig. 6, although the fluctuations are significant here.

Considering that permeance is influenced not only by the flow rate of

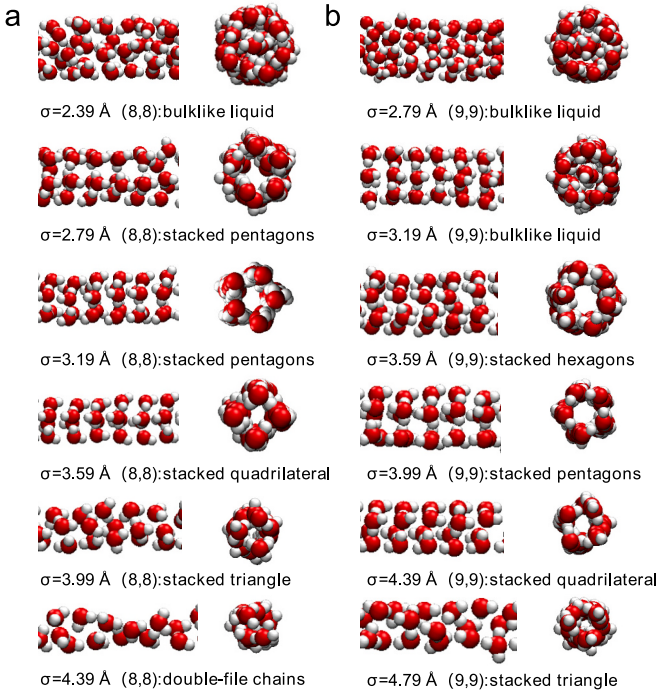

Fig. 9. Structures of water molecules at different σ values in single-walled (8) (a) and (9) (b) CNTs.

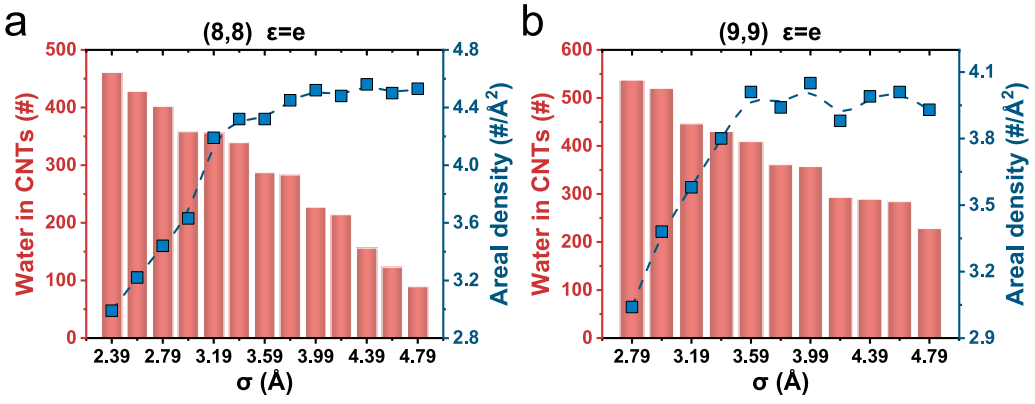

Fig. 8. The number of water molecules inside (8) (a) and (9) (b) CNTs as a function of σ.

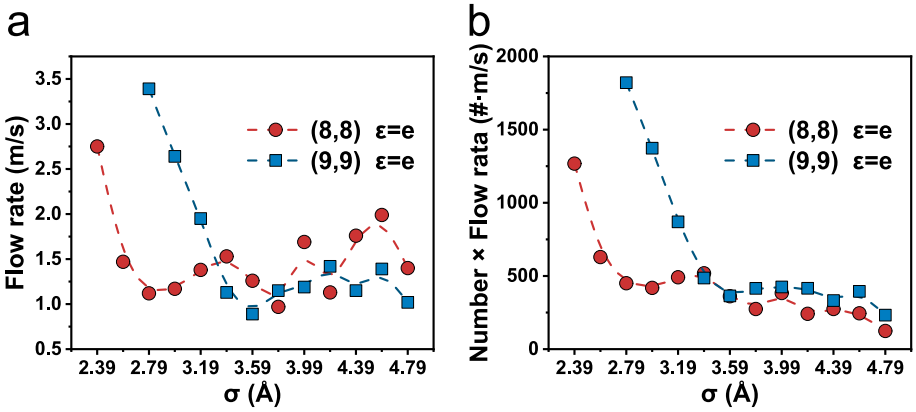

Fig. 10. The flow rate of water molecules (c), and the product of the number and flow rate of water molecules (d) as a function of σ.

water molecules inside CNTs but also by the number of water molecules inside them. Fig. 10b shows the coupled variation in the number and flow rate of water molecules inside the two types of CNTs with changing σ, demonstrating a similar trend with the results of permeance (Fig. 6), that is a sharp initial decrease followed by oscillations. This indicates that flow rate has a significant impact on water permeance compared to the density of water inside CNTs.

Combining with the microstructure analysis above, reducing σ makes the interior space of CNTs more spacious, allowing water molecules to flow more freely inside CNTs and facilitating the formation of more water chains, thereby increasing permeance. Conversely, increasing σ narrows the flow space inside CNTs, restricting the flow of water molecules inside CNTs, making it difficult for water molecules to form more water chains, thereby reducing permeance. This phenomenon explains why the number of water molecules inside CNTs decreases with increasing σ (Fig. 8), and the diameter of the water ring decreases with increasing σ (Fig. 7).

3.3. The influence of hydrophilicity on permeance

In the LJ potential function, another factor, hydrophilicity (ε), also affects the permeance. Fig. 11 illustrates the variation in permeance as ε increases from ε/8 to 8ε, with three different σ values selected for each type of CNTs. In the cases of (8) CNTs with σ values of 2.79, 3.39 and 3.59 Å, the permeance reaches its maximum at ε = e/8, with values of 5742.11, 3630.48 and 2577.12 LMHB, respectively. As ε increases, the permeance gradually decreases, reaching its minimum at ε = 8e, with values of 109.55, 35.08 and 50.28 LMHB, respectively (Fig. 11a). Similarly, for (9) CNTs with σ values of 2.99, 3.39 and 4.19 Å, the maximal permeance also locates at ε = e/8, with values of 6300.27, 3485.46 and 2025.19 LMHB, respectively. As ε increases, the permeance gradually decreases, reaching its minimum at ε = 8e, with values of 172.35, 8.96 and 77.98 LMHB respectively (Fig. 11b). For both types of CNTs, as ε rises from e/8 to 8e, the permeance gradually decreases.

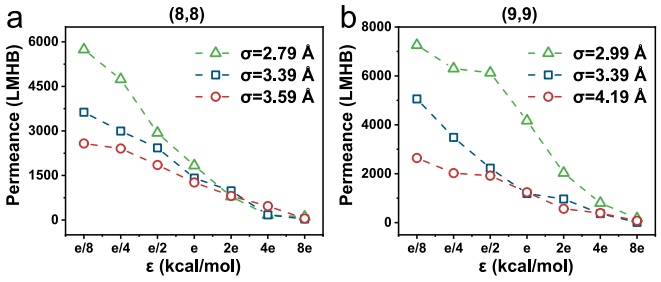

Fig. 11. The variation of permeance with ε for (8) (a) and (9) (b) CNTs at different σ values.

Due to the more pronounced decrease in permeance with increasing ε in (8) CNTs with σ of 3.59 Å and (9) CNTs with σ of 3.39 Å, we select these two σ values for further investigation of ε effect on water permeance. Firstly, we examine whether changing ε would affect the diameter of the water cluster inside CNTs.

Fig. 12 displays the density map of oxygen atoms of water in the *xy*-plane inside CNTs for different ε in the two types of CNTs. In both (8) and (9) CNTs with σ values of 3.59 and 3.39 Å, respectively, it is observed that the diameter of the water cluster inside CNTs remains unchanged at 4.6 and 6 Å, respectively, while ε increases from ε/8 to 8ε. Therefore, changing ε does not impact the diameter of the water cluster inside CNTs. However, as ε increases, the color of the water cluster gets darker in Fig. 12, indicating a higher density of water inside CNTs.

The variation curves of the number and density of water molecules inside CNTs of the two types of CNTs with respect to ε is illustrated in Fig. 13. The plane density of water molecules inside CNTs is calculated based on the diameter of the water cluster. In (8) CNTs with σ fixed at 3.59 Å, the number of water molecules inside CNTs gradually increases from 262 to 357, and the plane density of water molecules increases from 4.14 to 5.37 #/Å^2 while ε increases from ε/8 to 8ε. In (9) CNTs, when ε increases from ε/8 to 8ε with σ fixed at 3.39 Å, the number of water molecules inside CNTs gradually increases from 381 to 577, and the plane density of water molecules consequently increases from 3.35 to 5.1 #/Å^2. The number and plane density of water molecules inside both types of CNTs increase with increasing ε, explaining the darkened color of the water cluster in Fig. 12 with the increased ε. However, excessively high plane density of water molecules can increase the interaction forces between them, thereby increasing the resistance to motion inside the channel and leading to a decrease in permeance. This is consistent with the decrease in permeance shown in Fig. 11 as ε increases.

According to Werder et al.'s research, the hydrophilicity of the nanopores can be adjusted by keeping σ constant and altering the ε values of carbon atoms on the CNTs and oxygen atoms in water molecules [30]. Moreover, the changes in hydrophilicity have a significant impact on dynamic properties of water molecules inside nanotubes [19,22,43,44]. Consequently, it is possible to examine the effect of ε on the nanopore's hydrophilicity by analyzing the dynamic properties of water inside CNTs with varying ε. By analyzing the self-diffusion coefficient of water molecules along the *z*-axis (D_z), the dynamic behavior of water molecules inside CNTs can be characterized, indirectly measuring the hydrophilicity of the nanopores. To compute D_z, it is necessary to measure the mean squared displacement (MSD) of water molecules within the nanopores along the *z*-axis for all ε values, and then calculate D_z using the following formula:

$$D_z = \frac{\lim_{t\to\infty} \mathrm{MSD}_z}{2t} \tag{3}$$

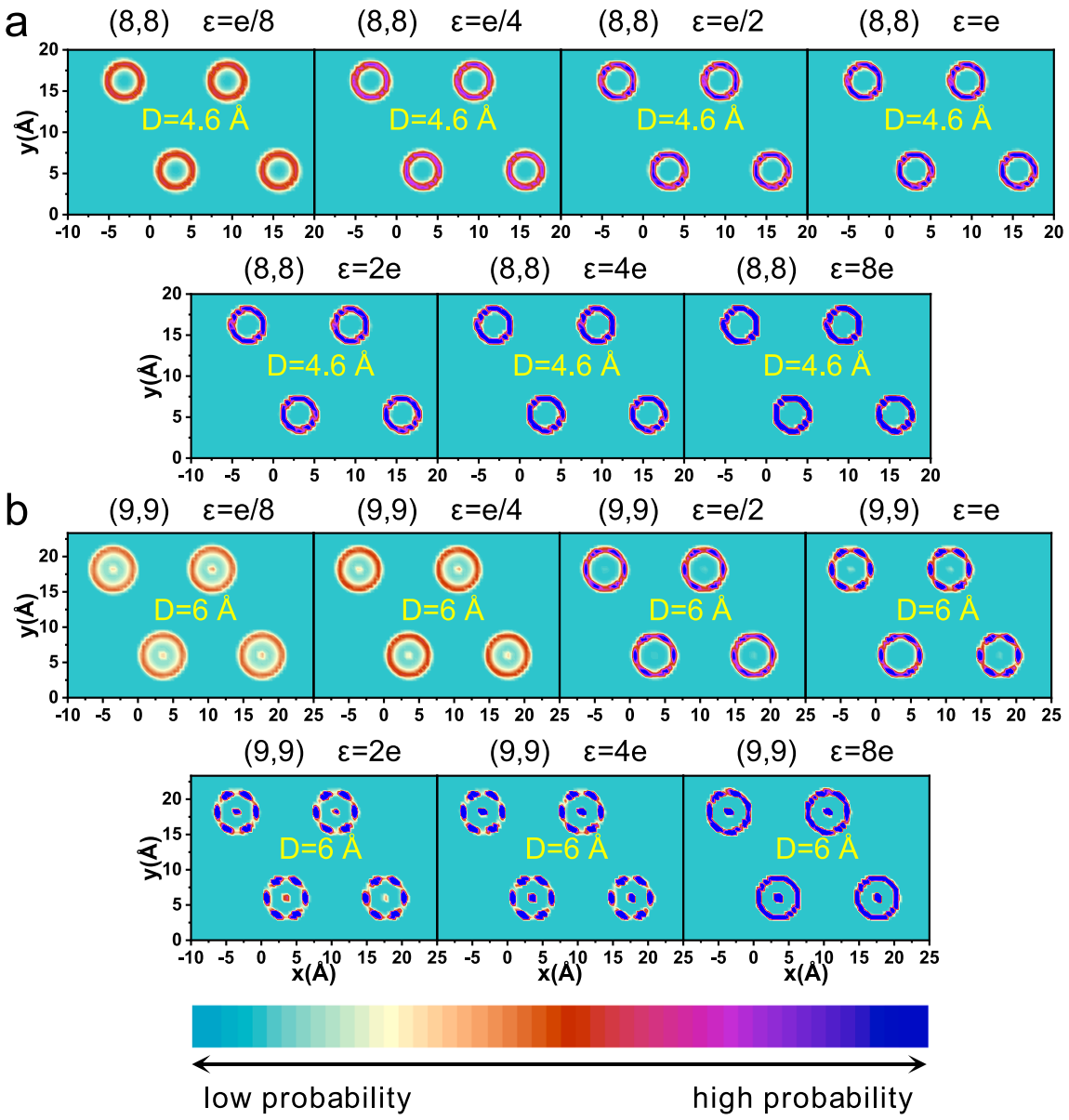

Fig. 12. The ε-dependent *xy*-plane density maps for oxygen atoms of water inside CNTs of (8) and (9) CNTs with σ values of 3.59 and 3.39 Å, respectively.

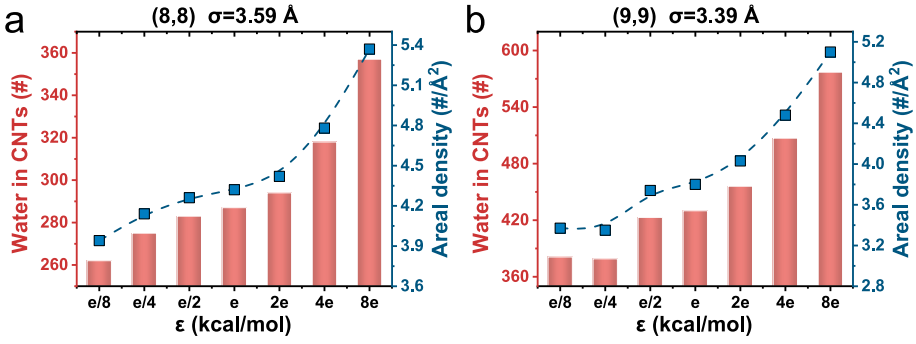

Fig. 13. Variation of the number and density of water molecules inside CNTs of (8) and (9) CNTs with respect to ε.

Figs. 14a&b present the ε-dependent MSD_z for (8) and (9) CNTs, respectively. The MSD_z plots exhibit linearity, while their slopes gradually decreasing as ε increases. Figs. 14c&d demonstrate the calculated D_z decreases with rised ε, suggesting that higher ε values enhance the hydrophilicity of CNTs. This results in increased resistance for water molecules passing through the CNTs, thereby reducing permeance, which aligns with findings in the literature [21]. The observation aligns with the phenomenon observed in Fig. 11, where permeance decreases

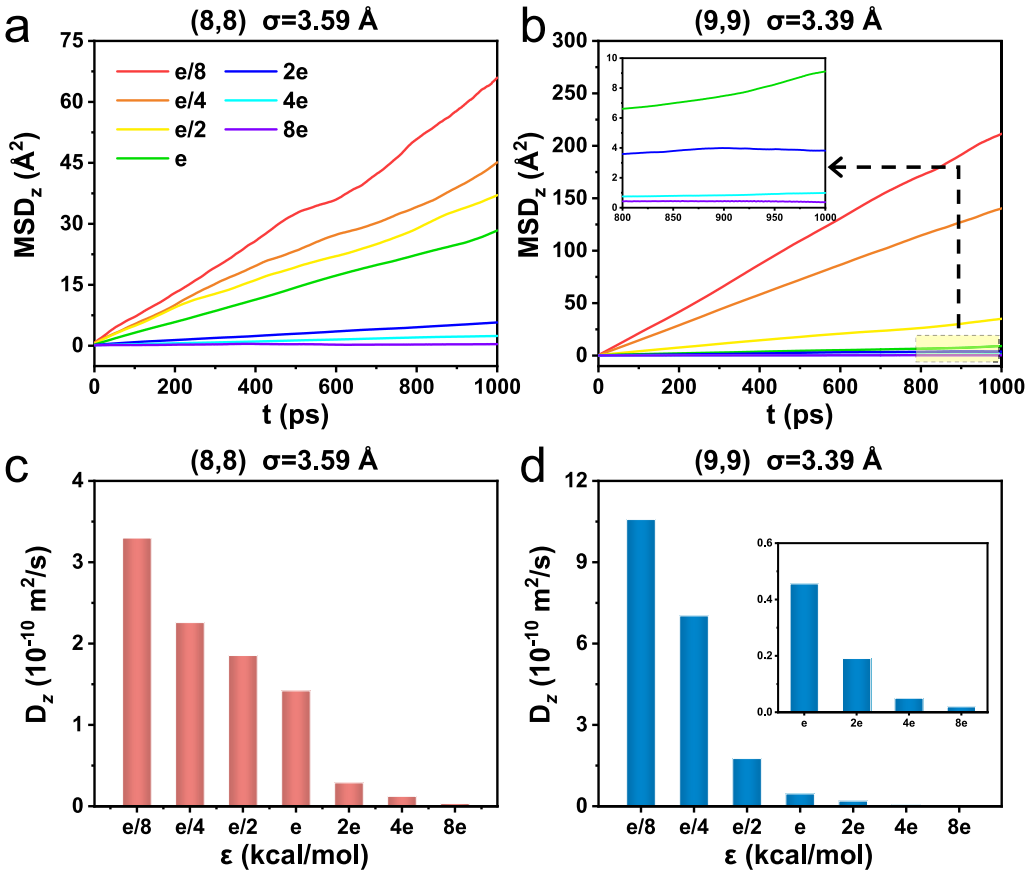

Fig. 14. Mean square displacement and self-diffusion coefficients of water molecules along the z-direction inside the nanotubes with (a and c) (8) and (b and d) (9) at different ε.

as ε increases.

Unlike (8) CNTs, the structure of water molecules in (9) CNTs changes with various ε. In some cases, the structure of water molecules is no longer a single-ring structure, but instead exhibits "ring+dot" structure. This structural change is not only related to ε, but also depends on the value of σ. Therefore, the microstructure of water molecules in CNTs is the result of the coupled effects of both σ and ε. It is necessary to study the coupling effect of these two factors. The relevant research will adopt ML methods for analysis in Section 3.5.

3.4. The influence of σ, ε and ΔP on ion rejection

Before introducing the findings from ML, we prefer to presenting the simulation results of ion rejections for all cases. Ion rejection (R) is usually defined as:

$$R = 1 - \frac{c_p}{c_f} \tag{4}$$

where c_p and c_f represent the ion concentrations on the feed side and permeate side, respectively. Herein, R of 100% means that the ions cannot pass through the CNTs, while R of 0 indicates that the ion concentration on the permeate side is equal to that on the feed side. In the pump method, due to the existence of periodic boundaries, there is no clear boundary between the feed side and the permeate side, and R can be calculated by:

$$R = 1 - \frac{F_i}{F_w} \Big/ \frac{n_i}{n_w} \tag{5}$$

where F_i and F_w represent the ion and water flux, respectively. F_i and F_w are calculated by counting the numbers of ions and water molecules passing through the CNTs during a certain simulation period. n_i and n_w represent the total number of ions and water molecules in each simulation case. It can be seen from Eq. (5) that R is closely related to water flux and ion flux. Since changes in σ and ε have a significant impact on permeance of water and ion, changing σ and ε will also have an impact on ion rejection.

Figs. 15a&b shows the variation of NaCl rejection in two types of CNTs with ε and σ. In (8) CNTs, while ε increases from e/8 to e/2 with σ kept at 2.79 Å, the NaCl rejection increases from 58.24% to 100%. As ε continues to increase, the rejection remains at 100%. In (9) CNTs, while ε increases from e/8 to e with σ kept at 3.19 Å, the NaCl rejection increases from 20.81% to 100%. As ε continues to increase, the rejection remains at 100% (Fig. 15a). Therefore, when ε increases from e/8 to 8e, the NaCl rejection gradually increases and then remains at 100%. Xu et al. have demonstrated that an increase in the hydrophilicity of the channels is beneficial for enhancing the rejection performance [32].

Since ion rejection is also influenced by pore size [8], and changing σ can change the effective diameter of CNTs, the impact of σ on R is examined. In (8) CNTs, when σ increases from 2.39 to 2.59 Å with ε kept at e, the rejection increases from 22.03% to 100%. As σ continues to increase, the rejection remains at 100%. In (9) CNTs, when σ increases from 2.79 to 3.39 Å with ε kept at e, the rejection increases from 37.97% to 100%. As σ continues to increase, the rejection remains at 100% (Fig. 15b). Therefore, when σ increases from 2.19 to 4.99 Å, the NaCl rejection gradually increases and then remains at 100%. When σ increases, the effective diameter of CNTs decreases and the diameter of the water ring inside the channel decreases, leading to a decrease in permeance but making ion passage through CNTs more difficult, thereby increasing the rejection.

Figs. 15c&d show the NaCl rejection as a function of ΔP for (8) and (9) CNTs under three different σ and ε conditions. As ΔP increases from

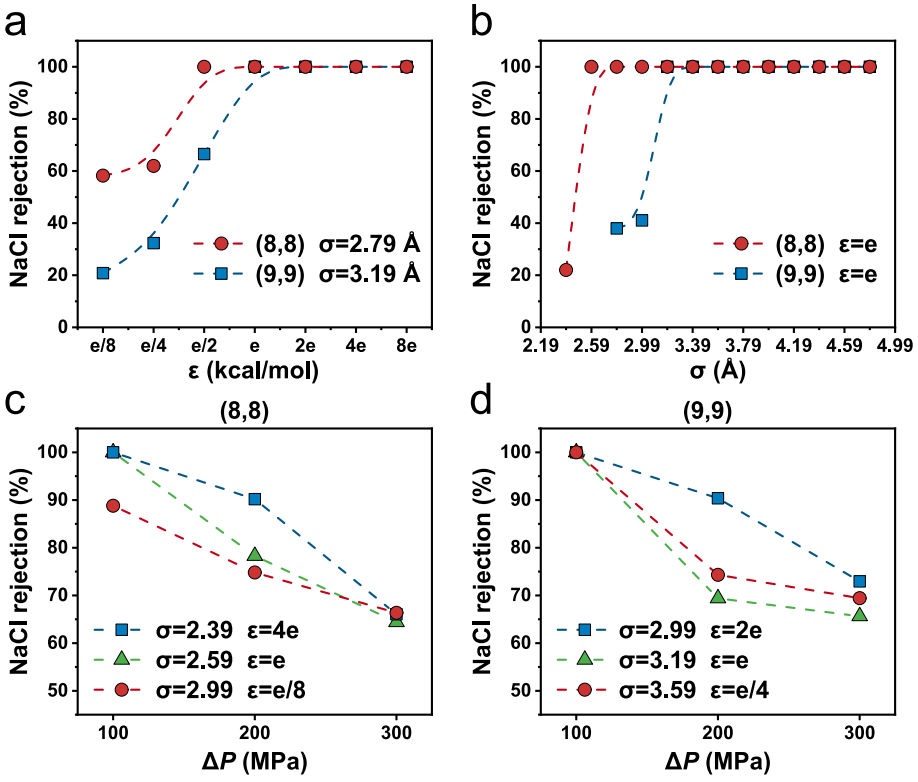

Fig. 15. NaCl rejection performance as a function of ε (a), and σ (b) while ΔP is 100 MPa. NaCl rejection performance as a function of ΔP for (8) (c) and (9) (d).

100 to 300 MPa, the NaCl rejection of both types of CNTs gradually decreases. This is consistent with the findings of Zhang et al., indicating that ion rejection decreases with increasing Δ*P* [45].

It is evident that ion rejection is simultaneously affected by σ, ε and Δ*P*. Subsequently, we then adopt a ML method to analyze the influence of the above three factors on permeance and rejection and find the optimal permeance when the rejection remains at 100%.

3.5. ML predicts optimal values

This work employs a two-step model combination approach, using Extreme Trees Regressor (ETR) and Gradient Boosting Classifier (GBC) to predict the highest permeance corresponding to a 100% ion rejection based on the permeance data obtained from HTMD calculations. Fig. 16 illustrates the process flow using σ, ε and Δ*P* as input features. In the process, ETR is first used to predict permeance, and the predicted permeance data from this model is used as one of the input features for GBC to predict the ion rejection using binary classification. A positive value is output for permeance when the ion rejection reaches 100%, otherwise a negative value is output to ensure that the optimization algorithm will discard parameters where the ion rejection does not reach 100%.

After the predictions are made, with permeance prediction from ETR and ion rejection prediction from GBC, these results are input into the Differential Evolution (DE) algorithm. DE then randomly generates input parameters σ, ε, and Δ*P* for ETR and GBC predictions. The permeance values are first evaluated. If the permeance is positive, it then checks whether the ion rejection is 100%. If the ion rejection is 100%, the current parameters are output; if not, DE adjusts the input parameters and recalculates permeance and ion rejection using ETR and GBC until a parameter combination that meets the criteria is found. If the permeance is negative, the parameters are adjusted directly and recalculated iteratively until the optimal solution is found.

This process not only improves the accuracy of predicting permeance and ion rejections under constrained conditions but also identifies the optimal operational conditions in practical applications through the optimization algorithm, providing effective methodological support for research and applications in related fields.

Using 70% of the data from the database as the training set for initial model construction, and the remaining 30% of the data is used as the test set to evaluate the model's predictive performance. Fig. 17 evaluates the predictive results of the ETR and GBC models. In line with numerous literature sources [46–48], the coefficient of determination (R2) is utilized to evaluate the goodness of fit for ETR, achieving an R2 of 0.961 (Fig. 17a), indicating effective predictive capability of the model for permeance. For the GBC model, following the methods in literature [49–51], performance in binary classification is evaluated using metrics such as accuracy, recall, and false positive rate (FPR) calculated from the confusion matrix. The classification threshold is set at 0.5, with ion rejections of 100% labeled as 1 (positive instances) and those below 100% labeled as 0 (negative instances). The results show that the model achieves a classification accuracy of 93.4% on the test set, with a recall of 0.98 and an FPR of 0.18. These performance metrics indicate that the GBC model performs well in this binary classification task (Fig. 17b).

The highest water permeance at 100% ion rejection in the existing data for (8) and (9) CNTs, the ML prediction those, and those by additional verification MD simulations are plotted in Fig. 18a. For the data obtained from HTMD, the (8) CNTs exhibit a maximum permeance of 3630.48 LMHB at 100% rejection, obtained at Δ*P* of 100 MPa, σ of 3.39 Å and ε of e/8. Similarly, the (9) CNTs show a maximum permeance of 2768.6 LMHB at 100% rejection, obtained at Δ*P* of 100 MPa, σ of 3.99 Å and ε of e/8. After prediction using EL and DE, the (8) CNTs achieve a permeance of 3653.5 LMHB at 100% rejection, obtained at Δ*P* of 110.94 MPa, σ of 3.12 Å and ε of e/7.49. For the (9) CNTs, the predicted permeance at 100% rejection is 3515.18 LMHB, obtained at Δ*P* of 112.47 MPa, σ of 3.71 Å and ε of e/7.68. Such prediction demonstrates that the strongly hydrophobic channel will promote the water permeance at the pore size around 10 Å, which is also found in the experimental work of Itoh et al. [52].

The ML predicted results are higher than those obtained from HTMD, warranting the verification of the ML results for accuracy. Using the

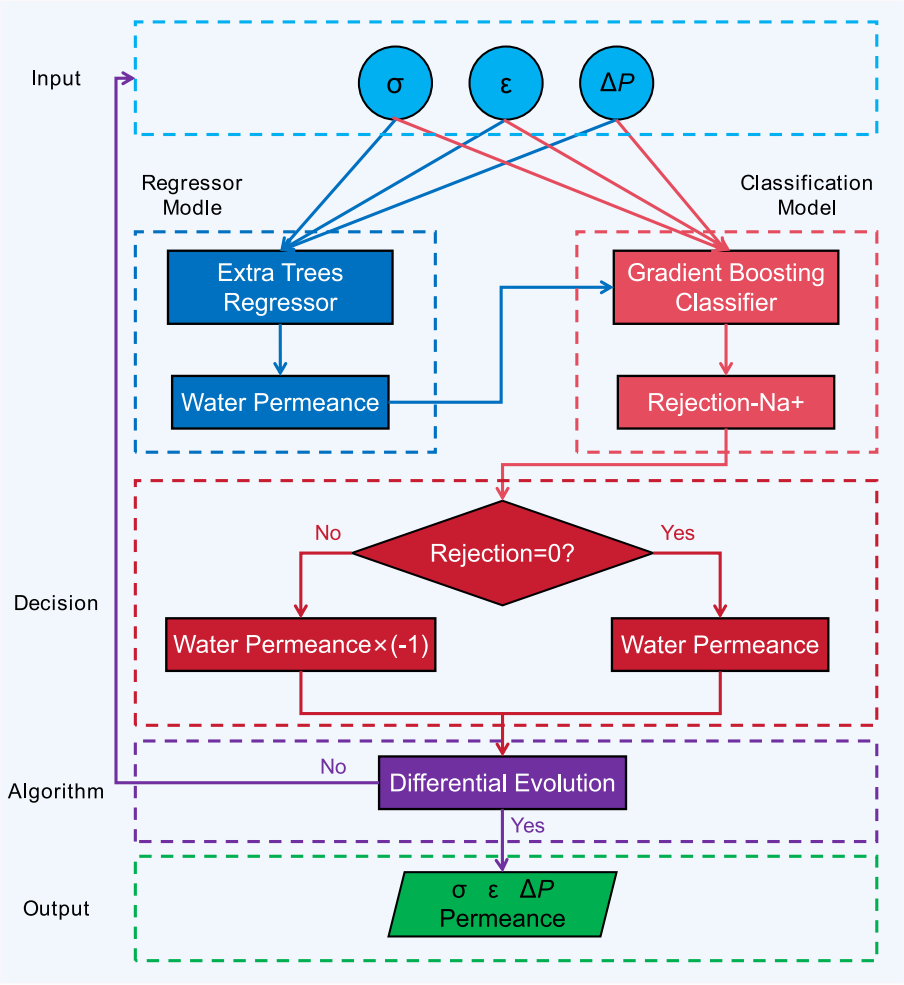

Fig. 16. Flowchart of the process for predicting the highest permeance model with 100% ion rejection using a two-step model combination method.

same simulation method, the predicted ΔP, σ and ε from ML are verified through additional MD simulations. The results indicate that under the predicted conditions from ML, both (8) and (9) CNTs achieve 100% ion rejection, with permeabilities of 3639.89 and 3508.95 LMHB, respectively. These values are higher than those from HTMD, but a little lower than the ML predictions by only 0.37% and 0.18%, respectively. This demonstrates the high accuracy of the ML model and its high feasibility.

Finally, the SHAP (SHapley Additive exPlanations) values are calculated to assess the impact of σ, ε and ΔP on permeance. SHAP is a method for explaining the predictions of ML models based on cooperative game theory and it can calculate the contribution of each feature to the model's prediction. Fig. 18b shows the SHAP values for the two types of CNTs, revealing that the permeance of both types of CNTs is most significantly influenced by σ, accounting for 53.19% and 58%, respectively. The influence of ε is secondary, at 45.73% and 40.84%, respectively. The impact of ΔP on permeance is minimal, at 1.08% and 1.16%, respectively. This indicates that σ is the primary factor determining permeance.

In SHAP analysis of rejection, it is found that for (8) CNTs, the rejection is most influenced by σ, accounting for 49.44%, followed by ε at 36.22%, with ΔP having the smallest impact at 14.34%. For (9) CNTs, the rejection is most influenced by ε, making up 48.73%, followed by σ at 35.78%, with ΔP having the smallest impact at 15.49%. This indicates that the ion rejection is more significantly affected by σ for CNTs with smaller diameters, while it is more significantly affected by ε for CNTs with larger diameters.

4. Conclusions

By conducting HTMD simulations on (8) and (9) CNTs, it is found that altering the pore size and hydrophilicity of CNTs significantly affects permeance and ion rejection. The number of water chains formed by intra-CNTs water molecules decreases with reduced pore size (increasing σ). Decreasing σ ($\sigma < \sigma_{C\text{-}O} = 3.19$ Å) effectively alters permeance, with permeance increasing as σ decreases and ion rejection also increases. Altering ε can effectively change the hydrophilicity of the pore, with hydrophilicity increasing of rising ε. The promoted hydrophilicity results in decreased permeance and increased ion rejection. Additionally, increasing ε leads to a rise in water molecule density within the pore, increasing water molecule transport resistance and reducing the permeance. Finally, using a two-step model combination method of ML to predict the highest permeance when ion rejection is 100%, the ML prediction results are highly consistent with simulation data. Furthermore, by evaluating the impact of σ, ε and ΔP on permeance using SHAP values, it is found that σ is the primary determinant of permeance, followed by ε, while ΔP has very little impact.

CRediT authorship contribution statement

Jinji Cao: Investigation, Data collection, Writing-original draft.
Zhaoqin Xu: Investigation, Machine learning analysis.
Mingjie Wei: Validation, Writing-review & editing, Funding Acquisition.
Lihan Li: Investigation, Discussion on machine learning.

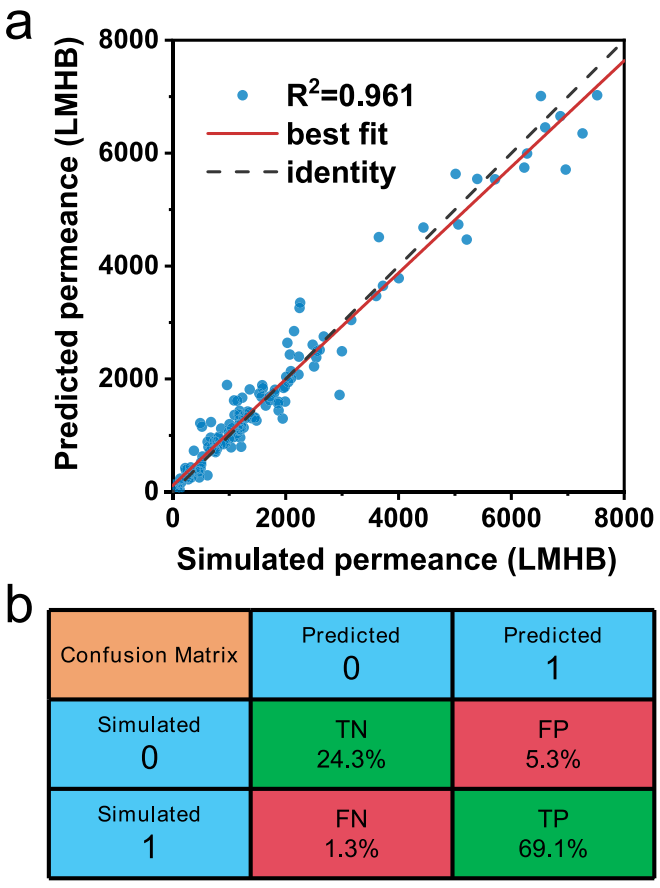

Fig. 17. (a) Results of the ETR model's predicted permeance. (b) Confusion matrix of the GBC model, where TP stands for true positive, TN for true negative, FP for false positive, and FN for false negative.

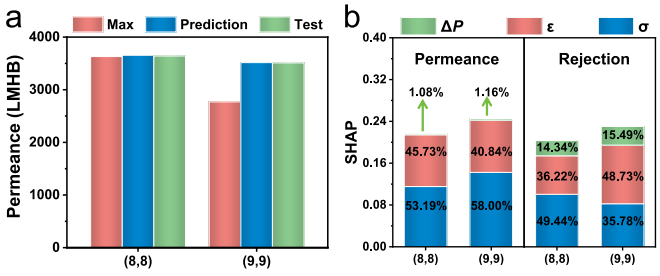

Fig. 18. (a) Permeance comparisons, "Max" indicates maximum permeance observed in the HTMD simulations, while "Prediction" and "Test" represent the predicted maximum permeance by ML and the permeance obtained by addition MD simulations with the parameters obtained from ML, respectively. (b) Contributions of ML predicted σ, ε and Δ*P* to the water permeance and ion rejection of (8) and (9) CNTs.

Bin Wu: Methodology, Discussion on machine learning, Validation. **Yong Wang:** Writing-review & editing, Supervision, Funding Acquisition.

All authors have approved to the final version of this manuscript.

Declaration of competing interest

The authors declare that they have no known competing financial interests or personal relationships that could have appeared to influence the work reported in this paper.

Acknowledgements

This work was financially supported by the National Key Research and Development Program of China (2022YFB3805201) and the National Natural Science Foundation of China (21921006, 22278206). The authors also thank the High Performance Computing Centre of Nanjing Tech University for supporting the computational resources.

Data availability

Data will be made available on request.

References

[1] G. Cao, M.M. Alam, A.Z. Juthi, Z. Zhang, Y. Wang, C. Jiang, T. Xu, Electrodesalination: state-of-the-art and prospective, Adv. Membr. 3 (2023) 100058, https://doi.org/10.1016/j.advmem.2022.100058.
[2] T.E. Culp, B. Khara, K.P. Brickey, M. Geitner, T.J. Zimudzi, J.D. Wilbur, S.D. Jons, A. Roy, M. Paul, B. Ganapathysubramanian, A.L. Zydney, M. Kumar, E.D. Gomez, Nanoscale control of internal inhomogeneity enhances water transport in desalination membranes, Science 371 (6524) (2021) 72–75, https://doi.org/10.1126/science.abb8518.
[3] S. Lin, Y. Zhang, L. Shao, C.H. Lau, Spray-assisted assembly of thin-film composite membranes in one process, Adv. Membr. 4 (2024) 100080, https://doi.org/10.1016/j.advmem.2023.100080.
[4] Z.Y. Xu, L.N. Zhang, L. Zhao, B.J. Li, B. Bhatia, C.X. Wang, K.L. Wilke, Y. Song, O. Labban, J.H. Lienhard, R.Z. Wang, E.N. Wang, Ultrahigh-efficiency desalination via a thermally-localized multistage solar still, Energy Environ. Sci. 13 (3) (2020) 830–839, https://doi.org/10.1039/c9ee04122b.
[5] Y.Z. Zhang, J.L. Sargent, B.W. Boudouris, W.A. Phillip, Nanoporous membranes generated from self-assembled block polymer precursors: quo Vadis? J. Appl. Polym. Sci. 132 (21) (2015) 41683, https://doi.org/10.1002/app.41683.
[6] G.J. Lin, J.M. Perez-Aguilar, Z.L. Gu, Molecular landscape on electrosorption improving the desalination performance using a mixed graphene oxide/graphene nitride membrane, J. Mol. Liq. 383 (2023), https://doi.org/10.1016/j.molliq.2023.122054.
[7] W.J. Zhao, L.J. Liang, Z. Kong, J.W. Shen, A review on desalination by graphene-based biomimetic nanopore: from the computational modelling perspective, J. Mol. Liq. 342 (2021), https://doi.org/10.1016/j.molliq.2021.117582.
[8] B. Corry, Designing carbon nanotube membranes for efficient water desalination, J. Phys. Chem. B 112 (5) (2008) 1427–1434, https://doi.org/10.1021/jp709845u.
[9] M. Elimelech, W.A. Phillip, The future of seawater desalination: energy, technology, and the environment, Science 333 (6043) (2011) 712–717, https://doi.org/10.1126/science.1200488.
[10] N. Ghaffour, T.M. Missimer, G.L. Amy, Technical review and evaluation of the economics of water desalination: current and future challenges for better water supply sustainability, Desalination 309 (2013) 197–207, https://doi.org/10.1016/j.desal.2012.10.015.
[11] K. Tarnacki, M. Meneses, T. Melin, J. van Medevoort, A. Jansen, Environmental assessment of desalination processes: reverse osmosis and Memstill, Desalination 296 (2012) 69–80, https://doi.org/10.1016/j.desal.2012.04.009.
[12] G. Hummer, J.C. Rasaiah, J.P. Noworyta, Water conduction through the hydrophobic channel of a carbon nanotube, Nature 414 (6860) (2001) 188–190, https://doi.org/10.1038/35102535.
[13] M. Majumder, N. Chopra, R. Andrews, B.J. Hinds, Nanoscale hydrodynamics - enhanced flow in carbon nanotubes, Nature 438 (7064) (2005) 44, https://doi.org/10.1038/43844a.
[14] E.Y.M. Ang, W. Toh, J. Yeo, R.M. Lin, Z.S. Liu, K.R. Geethalakshmi, T.Y. Ng, A review on low dimensional carbon desalination and gas separation membrane designs, J. Membr. Sci. 598 (2020) 117785, https://doi.org/10.1016/j.memsci.2019.117785.
[15] S. Ali, S.A.U. Rehman, H.Y. Luan, M.U. Farid, H.O. Huang, Challenges and opportunities in functional carbon nanotubes for membrane-based water treatment and desalination, Sci. Total Environ. 646 (2019) 1126–1139, https://doi.org/10.1016/j.scitotenv.2018.07.348.
[16] K. Goh, H.E. Karahan, L. Wei, T.H. Bae, A.G. Fane, R. Wang, Y. Chen, Carbon nanomaterials for advancing separation membranes: a strategic perspective, Carbon 109 (2016) 694–710, https://doi.org/10.1016/j.carbon.2016.08.077.
[17] Ihsanullah, Carbon nanotube membranes for water purification: developments, challenges, and prospects for the future, Sep. Purif. Technol. 209 (2019) 307–337, https://doi.org/10.1016/j.seppur.2018.07.043.
[18] B. Corry, Water and ion transport through functionalised carbon nanotubes: implications for desalination technology, Energy Environ. Sci. 4 (3) (2011) 751–759, https://doi.org/10.1039/c0ee00481b.
[19] J. Goldsmith, C.C. Martens, Molecular dynamics simulation of salt rejection in model surface-modified Nanopores, J. Phys. Chem. Lett. 1 (2) (2010) 528–535, https://doi.org/10.1021/jz900173w.
[20] F. Ebrahimi, A. Pishevar, Dependence of the dynamics of spontaneous imbibition into carbon nanotubes on the strength of molecular interactions, J. Phys. Chem. C 119 (51) (2015) 28389–28395, https://doi.org/10.1021/acs.jpcc.5b07883.
[21] S. Joseph, N.R. Aluru, Why are carbon nanotubes fast transporters of water? Nano Lett. 8 (2) (2008) 452–458, https://doi.org/10.1021/nl072385q.

[22] L.Y. Wang, R.S. Dumont, J.M. Dickson, Nonequilibrium molecular dynamics simulation of pressure-driven water transport through modified CNT membranes, J. Chem. Phys. 138 (12) (2013) 124701, https://doi.org/10.1063/1.4794685.
[23] Y.Y. Wang, Z.L. Cao, A.B. Farimani, Efficient water desalination with graphene nanopores obtained using artificial intelligence, Npj 2d Mater. Appl. 5 (1) (2021) 66, https://doi.org/10.1038/s41699-021-00246-9.
[24] L.J. Liang, H.X. Zhou, J.C. Li, Q. Chen, L.L. Zhu, H. Ren, Data-driven Design of Nanopore Graphene for water desalination, J. Phys. Chem. C 125 (50) (2021) 27685–27692, https://doi.org/10.1021/acs.jpcc.1c09470.
[25] J.W. Shen, Z. Kong, L. Zhang, L.J. Liang, Controlled interval of aligned carbon nanotubes arrays for water desalination: a molecular dynamics simulation study, Desalination 395 (2016) 28–32, https://doi.org/10.1016/j.desal.2016.05.024.
[26] S. Plimpton, Fast parallel algorithms for short-range molecular-dynamics, J. Comput. Phys. 117 (1) (1995) 1–19, https://doi.org/10.1006/jcph.1995.1039.
[27] H.J.C. Berendsen, J.R. Grigera, T.P. Straatsma, The missing term in effective pair potentials, J. Phys. Chem. 91 (24) (1987) 6269–6271, https://doi.org/10.1021/j100308a038.
[28] J.-P. Ryckaert, G. Ciccotti, H.J. Berendsen, Numerical integration of the cartesian equations of motion of a system with constraints: molecular dynamics of n-alkanes, J. Comput. Phys. 23 (3) (1977) 327–341, https://doi.org/10.1016/0021-9991(77)90098-5.
[29] R.W. Hockney, J.W. Eastwood, Computer simulation using particles, crc Press2021. doi:https://doi.org/10.1201/9780367806934.
[30] T. Werder, J.H. Walther, R.L. Jaffe, T. Halicioglu, P. Koumoutsakos, On the water-carbon interaction for use in molecular dynamics simulations of graphite and carbon nanotubes, J. Phys. Chem. B 107 (6) (2003) 1345–1352, https://doi.org/10.1021/jp0268112.
[31] I.S. Joung, T.E. Cheatham, Determination of alkali and halide monovalent ion parameters for use in explicitly solvated biomolecular simulations, J. Phys. Chem. B 112 (30) (2008) 9020–9041, https://doi.org/10.1021/jp8001614.
[32] F. Xu, M.J. Wei, Y. Wang, Effect of hydrophilicity on ion rejection of sub-nanometer pores, Sep. Purif. Technol. 257 (2021) 117937, https://doi.org/10.1016/j.seppur.2020.117937.
[33] X. Zhang, M.J. Wei, F. Xu, Y. Wang, Thickness-dependent ion rejection in nanopores, J. Membr. Sci. 601 (2020) 117899, https://doi.org/10.1016/j.memsci.2020.117899.
[34] X. Zhang, W. Zhou, F. Xu, M.J. Wei, Y. Wang, Resistance of water transport in carbon nanotube membranes, Nanoscale 10 (27) (2018) 13242–13249, https://doi.org/10.1039/c8nr03116a.
[35] F.Q. Zhu, E. Tajkhorshid, K. Schulten, Pressure-induced water transport in membrane channels studied by molecular dynamics, Biophys. J. 83 (1) (2002) 154–160, https://doi.org/10.1016/s0006-3495(02)75157-6.
[36] M.K. Borg, D.A. Lockerby, K. Ritos, J.M. Reese, Multiscale simulation of water flow through laboratory-scale nanotube membranes, J. Membr. Sci. 567 (2018) 115–126, https://doi.org/10.1016/j.memsci.2018.08.049.
[37] Z.L. Cao, V. Liu, A.B. Farimani, Water desalination with two-dimensional metal-organic framework membranes, Nano Lett. 19 (12) (2019) 8638–8643, https://doi.org/10.1021/acs.nanolett.9b03225.
[38] R. Upadhya, S. Kosuri, M. Tamasi, T.A. Meyer, S. Atta, M.A. Webb, A.J. Gormley, Automation and data-driven design of polymer therapeutics, Adv. Drug Deliv. Rev. 171 (2021) 1–28, https://doi.org/10.1016/j.addr.2020.11.009.
[39] F. Xu, M.J. Wei, X. Zhang, Y. Song, W. Zhou, Y. Wang, How pore hydrophilicity influences water permeability? Research 2019 (2019) 2581241, https://doi.org/10.34133/2019/2581241.
[40] J.R. Bordin, A. Diehl, M.C. Barbosa, Relation between flow enhancement factor and structure for Core-softened fluids inside nanotubes, J. Phys. Chem. B 117 (23) (2013) 7047–7056, https://doi.org/10.1021/jp402141f.
[41] X.F. Chen, Y. Qin, Y.D. Zhu, X.L. Pan, Y.Q. Wang, H.Y. Ma, R.X. Wang, C.D. Easton, Y. Chen, C. Tang, A.J. Du, A.S. Huang, Z.L. Xie, X.W. Zhang, G.P. Simon, M.M. B. Holl, X.H. Lu, K. Novoselov, H.T. Wang, Accurate prediction of solvent flux in sub-1-nm slit-pore nanosheet membranes, science, Advances 10 (17) (2024), https://doi.org/10.1126/sciadv.adl1455.
[42] J.A. Thomas, A.J.H. McGaughey, Water flow in carbon nanotubes: transition to subcontinuum transport, Phys. Rev. Lett. 102 (18) (2009) 184502, https://doi.org/10.1103/PhysRevLett.102.184502.
[43] B. Liu, R.B. Wu, J.A. Baimova, H. Wu, A.W.K. Law, S.V. Dmitriev, K. Zhou, Molecular dynamics study of pressure-driven water transport through graphene bilayers, PCCP 18 (3) (2016) 1886–1896, https://doi.org/10.1039/c5cp04976h.
[44] L. Ries, E. Petit, T. Michel, C.C. Diogo, C. Gervais, C. Salameh, M. Bechelany, S. Balme, P. Miele, N. Onofrio, D. Voiry, Enhanced sieving from exfoliated MoS2 membranes via covalent functionalization, Nat. Mater. 18 (10) (2019) 1112–1117, https://doi.org/10.1038/s41563-019-0464-7.
[45] X. Zhang, M. Wei, F. Xu, Y. Wang, Pressure-dependent ion rejection in nanopores, J. Phys. Chem. C 124 (37) (2020) 20498–20505, https://doi.org/10.1021/acs.jpcc.0c03641.
[46] J. Liu, A.W. Xiao, G.Y. Lei, G.F. Dong, M.T. Wu, Intelligent predicting of salt pond's ion concentration based on support vector regression and neural network, Neural Comput. & Applic. 32 (22) (2020) 16901–16915, https://doi.org/10.1007/s00521-018-03979-9.
[47] T. Sustersic, V. Gribova, M. Nikolic, P. Lavalle, N. Filipovic, N.E. Vrana, The effect of machine learning algorithms on the prediction of coating properties, ACS Omega 8 (5) (2023) 4677–4686, https://doi.org/10.1021/acsomega.2c06471.
[48] K.M. Katubi, M. Saqib, M. Maryam, T. Mubashir, M.H. Tahir, M. Sulaman, Z. A. Alrowaili, M.S. Al-Buriahi, Machine learning assisted designing of organic semiconductors for organic solar cells: high-throughput screening and reorganization energy prediction, Inorg. Chem. Commun. 151 (2023) 110610, https://doi.org/10.1016/j.inoche.2023.110610.
[49] Z.X. Sun, B.S. Jiang, X.L. Li, J.K. Li, K. Xiao, A data-driven approach for lithology identification based on parameter-optimized ensemble learning, Energies 13 (15) (2020) 3903, https://doi.org/10.3390/en13153903.
[50] Z.D. Wang, S.Q. Lou, S. Liang, X.Z. Sheng, Multi-class disturbance events recognition based on EMD and XGBoost in φ-OTDR, Ieee, Access 8 (2020) 63551–63558, https://doi.org/10.1109/access.2020.2984022.
[51] S. Rath, G.S. Priyanga, N. Nagappan, T. Thomas, Discovery of direct band gap perovskites for light harvesting by using machine learning, Comput. Mater. Sci. 210 (2022) 111476, https://doi.org/10.1016/j.commatsci.2022.111476.
[52] Y. Itoh, S. Chen, R. Hirahara, T. Konda, T. Aoki, T. Ueda, I. Shimada, J.J. Cannon, C. Shao, J. Shiomi, K. Tabata, H. Noji, K. Sato, T. Aida, Ultrafast water permeation through nanochannels with a densely fluorous interior surface, Science 376 (6594) (2022) 738–743, https://doi.org/10.1126/science.abd0966.